

# An Electron/Ion Dual-Conductive Alloy Framework for High-Rate and High-Capacity Solid-State Lithium-Metal Batteries

Chunpeng Yang, Hua Xie, Weiwei Ping, Kun Fu, Boyang Liu, Jiancun Rao, Jiaqi Dai, Chengwei Wang, Glenn Pastel, and Liangbing Hu\*

The solid-state Li battery is a promising energy-storage system that is both safe and features a high energy density. A main obstacle to its application is the poor interface contact between the solid electrodes and the ceramic electrolyte. Surface treatment methods have been proposed to improve the interface of the ceramic electrolytes, but they are generally limited to low-capacity or short-term cycling. Herein, an electron/ion dual-conductive solid framework is proposed by partially dealloying the Li–Mg alloy anode on a garnet-type solid-state electrolyte. The Li–Mg alloy framework serves as a solid electron/ion dual-conductive Li host during cell cycling, in which the Li metal can cycle as a Li-rich or Li-deficient alloy anode, free from interface deterioration or volume collapse. Thus, the capacity, current density, and cycle life of the solid Li anode are improved. The cycle capability of this solid anode is demonstrated by cycling for 500 h at 1 mA cm<sup>-2</sup>, followed by another 500 h at 2 mA cm<sup>-2</sup> without short-circuiting, realizing a record high cumulative capacity of 750 mA h cm<sup>-2</sup> for garnet-type all-solid-state Li batteries. This alloy framework with electron/ion dual-conductive pathways creates the possibility to realize high-energy solid-state Li batteries with extended lifespans.

Lithium-metal batteries have attracted increasing research interest due to their extremely high energy density.<sup>[1]</sup> While the Li-metal anode has been investigated for decades, its application has been mainly hampered by safety concerns resulting from the inevitable formation of Li dendrites on the anode during Li deposition.<sup>[2]</sup> The Li dendrites can not only impair the cell performance but also penetrate the separator and lead to internal short circuit, incurring safety concerns, particularly when flammable liquid electrolytes are used.<sup>[3]</sup> Solid-state batteries using solid-state electrolytes (SSEs) exhibit considerable advantages over liquid-electrolyte batteries in


terms of prohibiting Li dendrite penetration and improving the safety of the cell.<sup>[4]</sup> Various types of SSEs have been proposed, such as solid polymer electrolytes,<sup>[5]</sup> polymer–inorganic composite electrolytes,<sup>[6]</sup> and inorganic electrolytes.<sup>[7]</sup> Among them, ceramic SSEs have extremely high Young's moduli and rigidity to suppress Li dendrite penetration, and their nonflammability and non-leakage properties further enhance the safety of Li-metal batteries. Thus, SSEs are extensively utilized to endow Li-metal batteries with enhanced reliability and security,<sup>[8]</sup> particularly since the ionic conductivity of SSEs has been markedly improved. Numerous inorganic Li-ion conductors, such as oxides (garnets, perovskites, etc.), sulfides, and hydrides, have been reported with high ionic conductivity.<sup>[7]</sup> Among various SSEs, garnet-type Li<sub>7</sub>La<sub>3</sub>Zr<sub>2</sub>O<sub>12</sub> Li-ion conductor has attracted special interest because of its

high ionic conductivity, wide electrochemical stability window, and good chemical stability.<sup>[9]</sup>

However, a bottleneck in the development of solid-state batteries is the poor physical contact at the solid electrode–SSE interface.<sup>[10]</sup> The surface of garnet-type SSE is lithiophobic, especially when contaminants exist on the garnet surface, which results in poor Li–SSE contact and large interface impedance.<sup>[11]</sup> Some surface treatment methods, such as thin oxide coatings (e.g., Al<sub>2</sub>O<sub>3</sub>),<sup>[11a]</sup> surface alloying (e.g., Li–Si alloy),<sup>[11b,12]</sup> surface cleaning,<sup>[13]</sup> and surface chemical treating,<sup>[14]</sup> have been employed to improve the wettability of Li on the garnet SSE. These approaches have successfully reinforced the Li–garnet contact, reduced the interface impedance, facilitated the charge transfer across the interface, and remarkably improved the performance of solid-state Li batteries. However, such surface treatments are only effective at the Li–SSE interface. Further Li cycling from the bulk anode can cause the efficacy of the surface treatment to fail. As indicated in **Figure 1a**, although the interface modifying layer improves the interface contact of the pure Li with the garnet electrolyte, the volume change that incurs during cycling could generate interface gaps and even detach the Li anode from the SSE after large-capacity Li stripping or increased stripping/plating cycles, especially at high current densities. Stripping 1 mA h cm<sup>-2</sup> of Li would create a gap of ≈4.9 μm, based on the theoretical volumetric

Dr. C. Yang, H. Xie, W. Ping, Dr. K. Fu, B. Liu, Dr. J. Dai, Dr. C. Wang, G. Pastel, Prof. L. Hu  
Department of Materials Science and Engineering  
University of Maryland at College Park  
College Park, MD 20742, USA  
E-mail: binghu@umd.edu

Dr. J. Rao  
Advanced Imaging and Microscopy (AIM) Lab of Nano Center  
University of Maryland at College Park  
College Park, MD 20742, USA

 The ORCID identification number(s) for the author(s) of this article can be found under <https://doi.org/10.1002/adma.201804815>.

DOI: 10.1002/adma.201804815

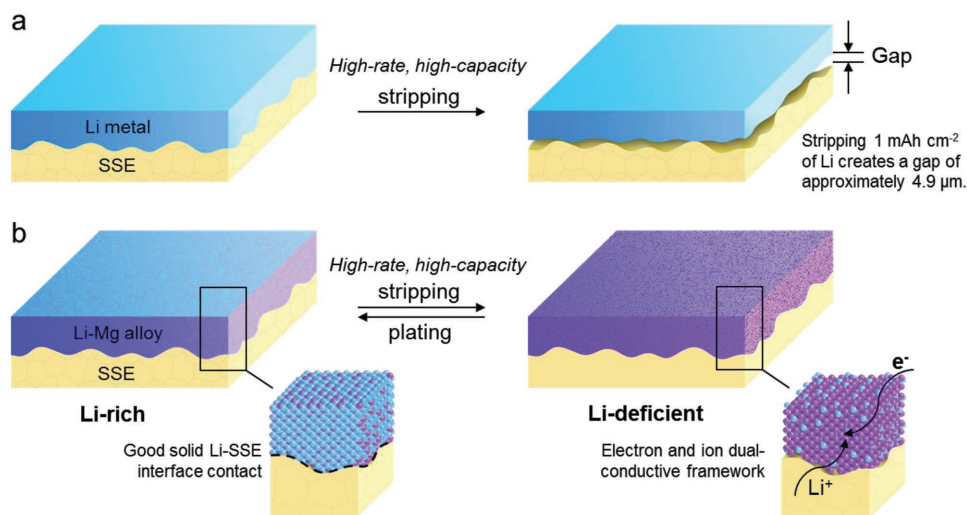


**Figure 1.** a,b) Schematics of the Li stripping/plating at high rate and high capacity in solid-state cells with a garnet-type SSE, using a pure Li-metal anode (a) and the Li–Mg alloy anode (b).

capacity of Li metal. Hence, a small Li capacity and short-term cycling is better suited for surface treatment methods in previously reported solid-state Li batteries. Moreover, the surface coating layer might not remain still during Li plating/stripping cycles.<sup>[12a]</sup> Side reactions between the SSE and Li anode can also lead to interphase formation and deteriorate the interfacial conductivity.<sup>[15]</sup> To improve the reversible capacity and cycle lifespan of Li-metal anodes with SSEs, efficient and durable Li-ion and electron conductive pathways must be constructed and maintained throughout cycling at the Li–SSE interface and throughout the entire Li-metal anode.

Herein, we show that a Li-ion and electron dual-conductive framework can be built by dealloying a Li–Mg alloy anode on a garnet electrolyte. As shown in Figure 1b, the Li-rich Li–Mg alloy is melted on the SSE and used as an anode. When a controlled amount of Li is stripped from the alloy anode, the Li–Mg alloy

becomes a Li-deficient material with a porous framework, but still maintains good interface contact with the garnet SSE. Because of the remaining Li in the alloy, the Li–Mg skeleton provides continuous pathways for both Li ions and electrons. Superior to previous surface treatment methods, the ion/electron dual-conductive solid framework serves as an effective host for the Li anode even if a large capacity of Li is stripped. Thus, the ion/electron dual-conductive framework derived from the Li alloy provides a high-capacity solid-state Li-metal anode with a long cycle life.

Mg was selected as the alloy framework because it is low density ( $1.7 \text{ g cm}^{-3}$ ), and miscible with Li at a moderately high temperature and a wide concentration range.<sup>[16]</sup> To form the initial Li–Mg alloy, we heated the Li with 20 wt% of Mg metal (approximately  $\text{Li}_{0.93}\text{Mg}_{0.07}$ ) at  $350 \text{ }^\circ\text{C}$  in an argon-filled glove box and then cooled the alloy to room temperature. As shown in the Li–Mg binary phase diagram (Figure 2a),<sup>[16]</sup> after cooling

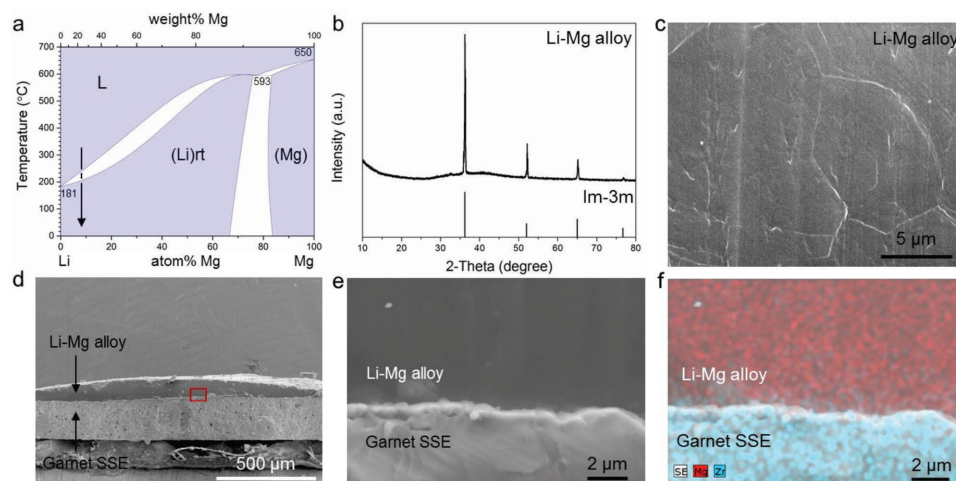


**Figure 2.** Li–Mg alloy on the garnet SSE. a) Phase diagram of Li–Mg. The arrow shows the concentration of Mg and the solidifying process in this work. a) Reproduced with permission.<sup>[16]</sup> Copyright 2001, Springer Nature. b) XRD profile of the Li–Mg alloy in comparison with standard body-centered cubic Li (JCPDS 89-3940, space group  $Im\bar{3}m$ ). c) SEM image of the Li–Mg alloy. d) Cross-sectional SEM image of the Li–Mg alloy melted on the garnet SSE. e) High-magnification cross-sectional SEM image and f) corresponding elemental mapping by EDX at the alloy–garnet interface.

to room temperature, Li and Mg form a solid solution, which is structurally similar to Li with a space group of  $Im\bar{3}m$ . The X-ray diffraction (XRD) profile of the Li–Mg alloy (Figure 2b) confirmed the body-centered cubic phase of the Li–Mg solid solution (space group:  $Im\bar{3}m$ ), which is the same structure as Li metal (JCPDS 89-3940). The cell size of the Li–Mg is 3.514 Å, as derived from XRD refinement, which approximates the cell size of Li (3.509 Å). The similar structure of the Li–Mg solid solution to Li metal prevents phase transformation during electrochemically plating/stripping of Li, free from structural fracture. A scanning electron microscopy (SEM) image of the Li–Mg alloy (Figure 2c) shows a dense morphology. Mg distributes homogeneously in the Li–Mg alloy without agglomeration (see the uniform Mg elemental distribution in Figure S1, Supporting Information) or residual metallic Mg (not observed by XRD in Figure 2b).

The SSE is a garnet-type  $\text{Li}_{6.75}\text{La}_3\text{Zr}_{1.75}\text{Ta}_{0.25}\text{O}_{12}$  dense pellet, which was polished to  $\approx 300\ \mu\text{m}$  thick prior to use. The garnet SSE was found to be better wetted by several Li-metal alloys (such as Li–Sn alloy) than pure Li metal,<sup>[12b,17]</sup> and we observed that our Li–Mg alloy also demonstrated good wetting on the garnet SSE. The molten Li–Mg alloy shows a small contact angle on the garnet SSE (Figure S2, Supporting Information). As shown in the digital photo (Figure S3, Supporting Information) and cross-sectional SEM images (Figure 2d,e), Li–Mg alloy adheres to the garnet SSE surface firmly after melting and solidifying the Li–Mg alloy on the garnet surface. The alloy and garnet form a close interface contact without any noticeable gaps between the alloy and solid electrolyte (Figure 2e), in contrast to the poor interface contact of pure Li melted on the garnet SSE via the same method (Figure S4, Supporting Information). The energy-dispersive X-ray spectroscopy (EDX) elemental mapping of Mg and Zr clearly shows that the Li–Mg alloy attached to the garnet surface and Mg uniformly dissolved in the dense solid solution alloy. The seamless interface contact between the anode and SSE is the first step toward the durable solid-state Li anode.

The electron/ion dual-conductive solid framework is obtained by partially dealloying Li from the Li–Mg solid solution to form a Li-deficient alloy, in which a controlled capacity of Li is stripped and the remaining Li in the skeleton conducts both electrons and Li ions. The voltage profile of electrochemically stripping Li from the Li-rich Li–Mg alloy is shown in Figure 3a, exhibiting a relatively stable plateau with a small overpotential of 10–15 mV. We note that the voltages are versus  $\text{Li}^+/\text{Li–Mg}$  alloy. The voltage of a Li-rich Li–Mg alloy is  $\approx 0\ \text{V}$  versus  $\text{Li}^+/\text{Li}$  and the average voltage for lithiation/delithiation of the Li–Mg alloy is 0.0325 V versus  $\text{Li}^+/\text{Li}$ .<sup>[18]</sup> The maximum available capacity of the alloy anode mainly depends on its thickness. In Figure 3a, a total capacity of 5.5 mA h was charged until a spike in voltage appeared, which indicates the complete depletion of Li—an equivalent of 1.4 mg of Li dealloyed from the pristine Li–Mg alloy.

The impedance before and after exhaustion of Li from the Li–Mg alloy was investigated by electrochemical impedance spectroscopy (EIS; Figure 3b). The Nyquist plots of the Li–Mg | garnet SSE | Li–Mg cell before and after depleting Li metal both show two semi-circles. The semi-circles are attributed to the impedance of the garnet SSE (high frequency range,  $R_1$ ) and

the interface resistance (low frequency range,  $R_2$ ),<sup>[13]</sup> as simulated by the equivalent circuit shown in Figure 3b. The impedance of the garnet SSE demonstrated no significant change after stripping Li from the anode. The interface impedance increased after completely stripping Li because the effective Li–garnet contact area is reduced, but only from 142 to 295  $\Omega\ \text{cm}^2$ . This could hardly be achieved using a pure Li-metal anode. For a pure solid Li anode without the dual-conductive framework, the anode would collapse after completely depleting Li metal, resulting in an increase of interfacial resistance by orders of magnitude.

In practical cells, the anode is not designed to be completely depleted of Li. Rather, only partially stripping Li from the Li-rich alloy by controlling the capacity of Li results in the formation of a Li-deficient Li–Mg alloy framework. The remaining Li in the Li-deficient alloy skeleton can then conduct both electrons and Li ions, thus serving as an ideal dual-conductive host for the Li-metal anode. Figure 3c shows the SEM image of the Li-deficient alloy after stripping 2 mA h  $\text{cm}^{-2}$  of Li. The resulting alloy is Li-deficient and porous compared with the pristine Li–Mg alloy (Figure 2c), but maintains an interconnected structure and good contact with the garnet SSE (see the cross-sectional SEM image in Figure S5 in the Supporting Information), serving as an electron and ion conductive host for Li deposition. For the pure Li-metal anode, stripping 2 mA h  $\text{cm}^{-2}$  of Li means generating a gap of  $\approx 10\ \mu\text{m}$  between the anode and the garnet SSE, which would drastically increase the interface impedance and lead to cell failure. Our previous study revealed that a thin Mg coating layer on the garnet does not stay at the interface but rather dissolves in the bulk Li anode after cycling.<sup>[12a]</sup> Consistently, in this work the Mg skeleton remains uniform in the Li-deficient anode after Li stripping, not cumulated at the interface, as evidenced by EDX elemental mapping (Figure 3d).

To clearly observe the change of the Li in the alloy framework, we conducted time-of-flight secondary ion mass spectroscopy (ToF-SIMS) on the cross-section of the alloy–SSE interface and mapped the intensity of the different elements before and after Li stripping. The elemental distribution of La, Li, and Mg in Figure 3e shows that the pristine Li-rich alloy on the garnet contains highly concentrated Li metal in the alloy before cycling. The intensity of Mg was much lower compared with Li. After electrochemically depleting Li from the alloy anode, the intensity of Li is significantly reduced (Figure 3f), forming a Li-deficient Li–Mg alloy. In contrast, the intensity of Mg remains unchanged after dealloying Li, indicating the stability of Mg as the anode framework. The Li-deficient Li–Mg alloy framework is expected to maintain the topological feature and microstructure of the electrode after Li stripping.

In the Li plating process, Li is plated in the Li-deficient alloy framework and recovers the Li-rich alloy. The SEM images (Figure S6, Supporting Information) show that the Li–Mg alloy after a Li stripping/plating cycle became a relatively dense Li-rich alloy, compared with the Li-deficient alloy after Li stripping (Figure 3c and Figure S5, Supporting Information). No Li dendrites were observed after Li plating. The Li-plated alloy shows a consistent morphology on the surface and throughout the cross section. Li did not accumulate on the surface of the Li–Mg alloy framework or at the alloy–garnet interface, but formed



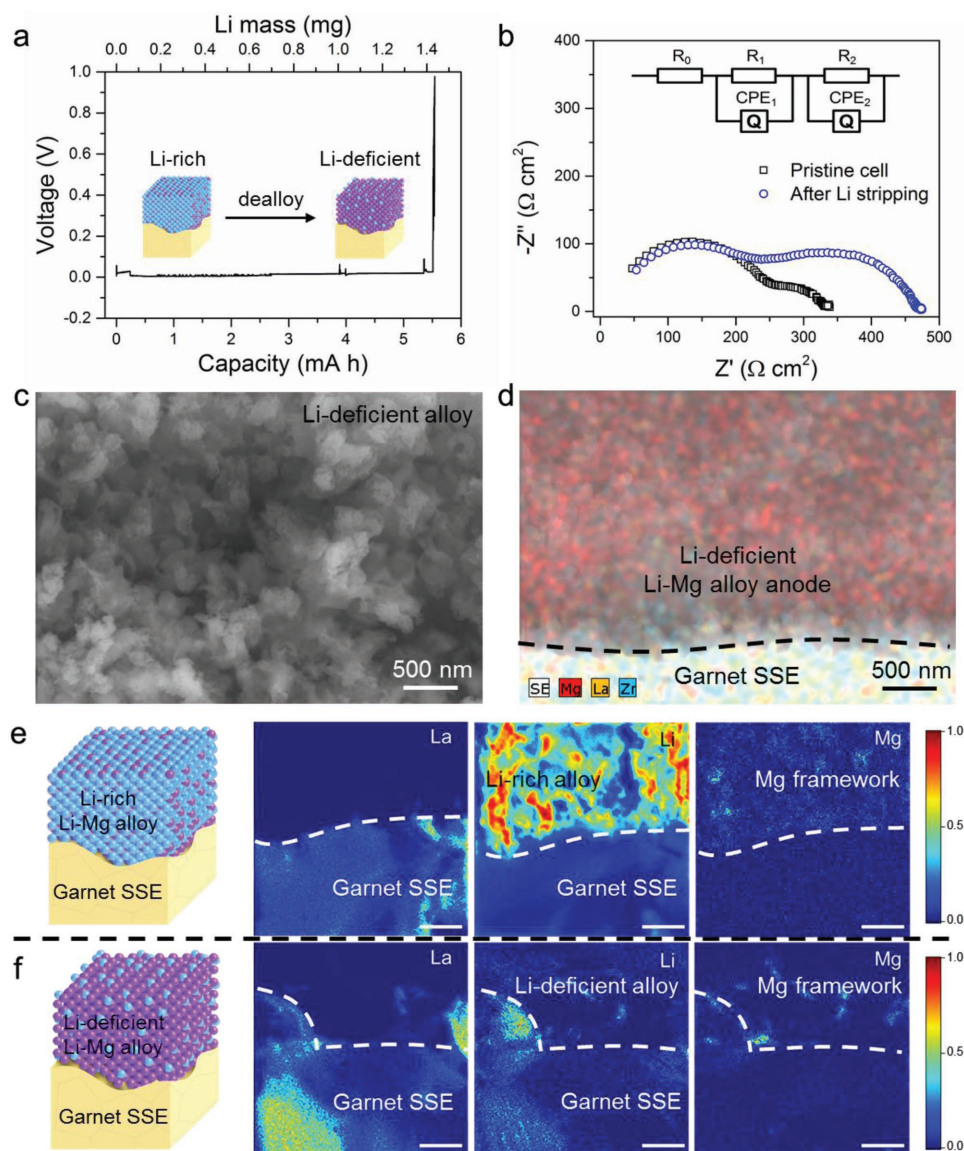


**Figure 3.** Plating/stripping behavior of Li within the Li–Mg alloy framework. a) Voltage profile of Li stripping from the Li-rich Li–Mg alloy anode on the garnet SSE at  $0.5 \text{ mA cm}^{-2}$ . The voltages are versus  $\text{Li}^+/\text{Li-Mg alloy}$ . b) Nyquist plots of the symmetric Li–Mg | garnet SSE | Li–Mg solid-state cell tested at room temperature before and after stripping Li from the Li–Mg anode. c) Top view and d) cross-sectional SEM image with elemental mapping of the Li-deficient Li–Mg alloy after electrochemically dealloying the anode on the garnet SSE. e,f) Elemental mapping of La, Li, and Mg by ToF-SIMS at the cross section of the alloy–garnet interface of the Li-rich Li–Mg alloy before cell cycling (e) and the Li-deficient Li–Mg alloy after stripping Li (f). Scale bars in (e) and (f):  $2 \mu\text{m}$ . The color intensity in (e) and (f) indicates the normalized counts per ToF-extraction.

a uniform Li-rich alloy, indicating the reversibility of Li plating/stripping within the alloy framework.

The solid electron/ion dual-conductive framework remarkably enhances the cycling life and the areal capacity of the Li-metal anode in the solid-state battery. As shown in **Figure 4a**, the Li–Mg alloy anode demonstrates stable cycling performance at  $1 \text{ mA cm}^{-2}$  for 250 cycles, with a capacity of  $1 \text{ mA h cm}^{-2}$  in each half cycle (i.e., plating/stripping for 1 h in each half cycle). The cell was further cycled at  $2 \text{ mA cm}^{-2}$ , which is a high current density for an all-solid-state battery, for 250 more cycles and  $2 \text{ mA h cm}^{-2}$  each half cycle (**Figure 4b**), totally 1000 h cycling. After the 1000 h cycling at 1 and  $2 \text{ mA cm}^{-2}$ , a high cumulative plating capacity of  $750 \text{ mA h cm}^{-2}$  was realized. The

Li anode within the solid dual-conductive Li–Mg framework shows smooth plating/stripping voltages (insets in **Figure 4a,b**). A small overpotential is observed throughout the long-term cycling (**Figure 4c**), indicating that the alloy framework is durable enough to prevent interface detachment and significant volume changes.

There is a concern that some solid-state Li-metal batteries in the literature could actually form soft short circuits.<sup>[19]</sup> Thus, we investigated the impedance evolution of the solid-state cell featuring the Li–Mg alloy framework. The impedance before cycling and after 500 and 1000 h cycling are plotted and fitted by the equivalent circuit in **Figure 4d**. Even after 1000 h of cycling, the cell continues to show two semi-circles in the Nyquist plot,

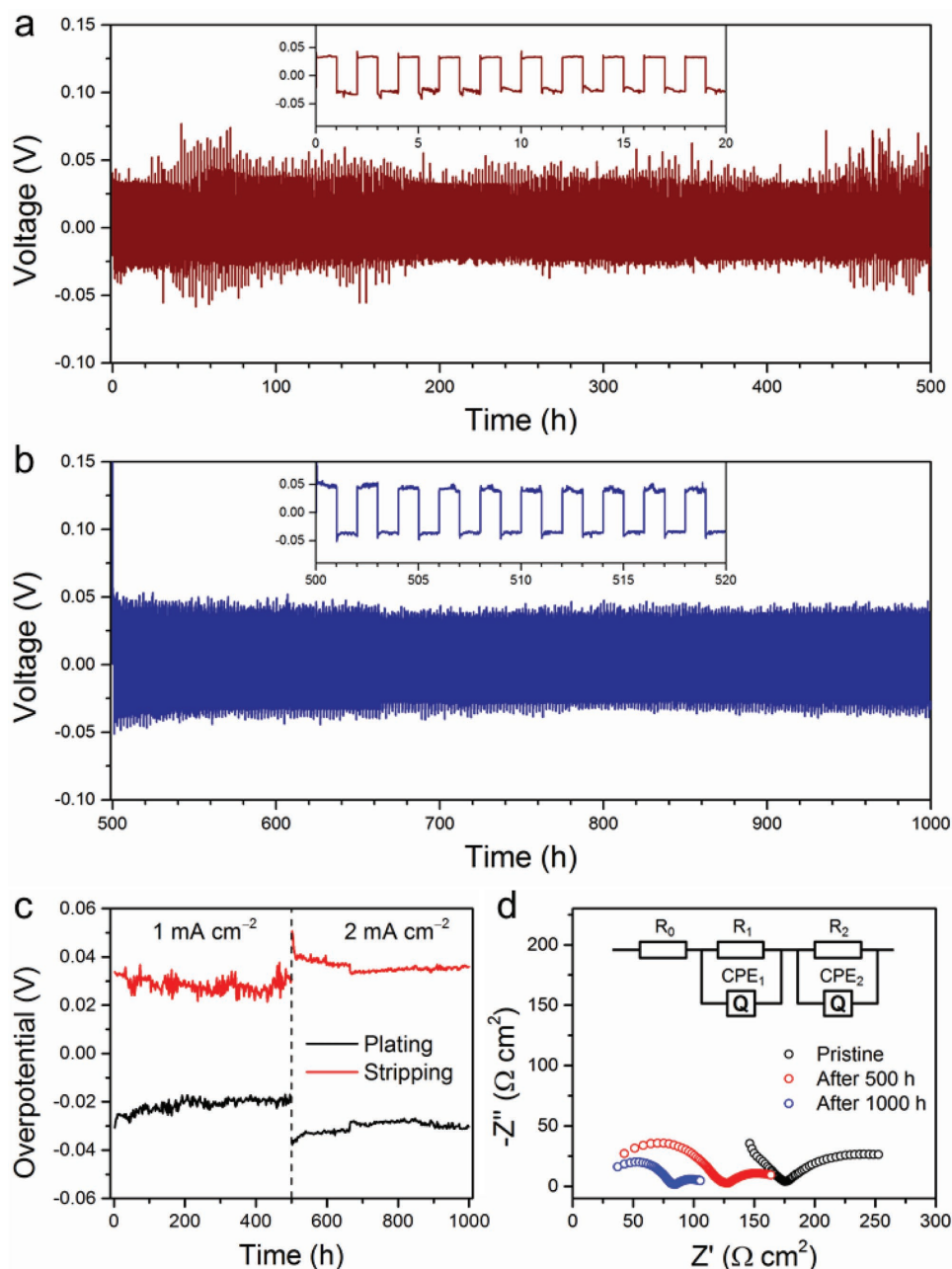


**Figure 4.** Electrochemical performance of the Li-Mg alloy anode. a,b) Voltage profile of Li cycling at room temperature in a symmetric Li-Mg | garnet SSE | Li-Mg solid-state cell at 1 mA cm<sup>-2</sup> for 1 h in each half cycle for a total of 500 h (a), followed by 2 mA cm<sup>-2</sup> for 1 h in each half cycle for another 500 h (b). c) Average overpotentials during Li plating/stripping at 1 and 2 mA cm<sup>-2</sup>. d) Nyquist plots of the solid-state symmetric cell before cycling, after cycling at 1 mA cm<sup>-2</sup> for 500 h, and after cycling at 2 mA cm<sup>-2</sup> for additional 500 h.

similar to the EIS before the long-term cycling (Figure 3b). This indicates the anode-garnet interface has not deteriorated over the prolonged cycling. Instead, the interface impedance ( $R_2$  in the equivalent circuit) reduced from the pristine 117 to 58  $\Omega \text{ cm}^2$  after 500 h cycling, and further decreased to 35  $\Omega \text{ cm}^2$  after 1000 h cycling, suggesting that the dual-conducting alloy framework prevents short-circuiting and enhances the lifespan of the solid-state Li battery. SEM images (Figure S7, Supporting Information) of the Li-Mg alloy after the cycling confirm that the alloy remains relatively intact with good interface contact

with the garnet SSE, without Li dendrite penetration, further substantiating the outstanding advantage of the solid dual-conductive alloy anode.

In solid-state Li batteries, the per-cycle areal capacity (i.e., the areal capacity of Li plated for each cycle), the current density during plating/stripping, and the cumulative capacity of the plated Li prior to short circuit or cell failure are considered important parameters for evaluating the cycling performance of solid-state Li anodes.<sup>[19]</sup> In Figure 5, we compare these parameters of the solid-state Li anode demonstrated in this work with

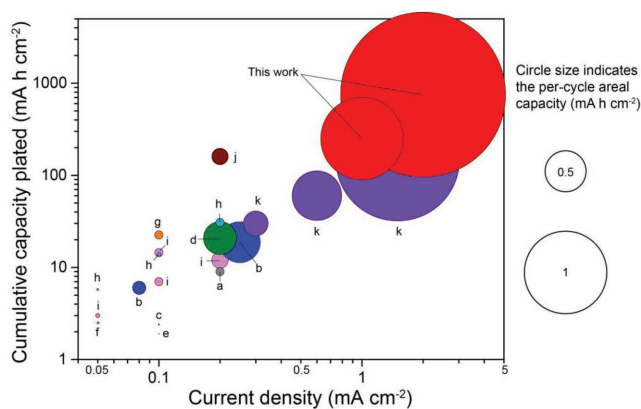


**Figure 5.** The cycling performances of Li-metal anodes in solid-state batteries. The plot summarizes the current density (*x*-axis), cumulative areal plating capacity (*y*-axis), and per-cycle areal capacity of the Li-metal anode (size of each circle) in this work and in prior publications using solid inorganic electrolytes. Thin-film cells (due to low areal capacity) and cells using liquid electrolytes (or liquid–solid hybrid electrolytes), polymer electrolytes, or 3D solid electrolytes are not included in the figure. Points and references include: a) ref. [11a], b) ref. [12b], c) ref. [20], d) ref. [13], e) ref. [12a], f) ref. [17] g) ref. [14], h) ref. [21], i) ref. [22], j) ref. [7e], k) ref. [7f]. The cell in this work was tested at room temperature whereas some literature results were obtained at elevated temperature (e.g., point k was tested at 25, 60, and 100 °C from left to right). The details of the references are summarized in Table S1 in the Supporting Information. Each work is plotted as points with the same color, of which each circle represents a particular cycling current density (e.g., the two red circles represent cycling performance at 1 and 2 mA cm<sup>-2</sup> in this work).

those of recent publications (data points a–k) that use planar and solid inorganic electrolytes (a–g, dense planar garnet SSEs<sup>[11a,12–14,20]</sup>; h, garnet–polymer composite electrolyte<sup>[21]</sup>; i, LiZr<sub>2</sub>(PO<sub>4</sub>)<sub>3</sub><sup>[22]</sup>; and j and k, sulfide SSEs<sup>[7e,f]</sup>; see Table S1 in the Supporting Information for more details). Lacking interface stability and volume sustainability during cycling, these previously reported solid-state Li anodes were cycled at small current densities with low cumulative capacities that are still far from meeting the needs of practical applications. In comparison, our Li-metal anode, benefiting from the electron/ion dual-conductive framework of the partially dealloyed Li–Mg alloy, exhibits outstanding cycling performance. The Li anode can cycle at high current densities (1 and 2 mA cm<sup>-2</sup>) and demonstrates large per-cycle areal capacities (up to 2 mA h cm<sup>-2</sup>) for a cumulative plating capacity of 750 mA h cm<sup>-2</sup>, which is to the best of our knowledge the record high cumulative capacity for Li anodes using planar inorganic SSEs. Moreover, the EIS in Figure 4d shows that the cell does not short circuit after 1000 h cycling (750 mA h cm<sup>-2</sup>), further proving the reliability and safety of the solid-state battery with the e<sup>-</sup>/Li<sup>+</sup> dual-conductive framework. Although the use of the Li–Mg alloy reduces the battery energy density, the decrease is slight because the portion of Mg can be small and the density of Mg is low (1.7 g cm<sup>-3</sup>). In this work, we used 20 wt% Mg in the Li–Mg alloy. The theoretical specific capacity decreases from 3860 mA h g<sup>-1</sup> (pure Li metal) to 3088 mA h g<sup>-1</sup> (Li–Mg alloy). The decrease in theoretical volumetric capacity density is even smaller, from 2046 mA h cm<sup>-3</sup> (pure Li metal) to 1898 mA h cm<sup>-3</sup> (Li–Mg alloy). The energy density of the battery using the Li–Mg alloy anode is appealing since the dual-conductive alloy

framework greatly augments the practical areal capacity of the solid Li anodes.

We have demonstrated an electron/ion dual-conductive framework as the Li-metal host in a solid-state battery by electrochemically dealloying Li from a Li–Mg alloy anode. The Li–Mg solid solution allows Li stripping and plating within the alloy framework to form Li-deficient and Li-rich alloys that conduct both electrons and Li-ions. The alloy anode forms seamless interface contact with the garnet-type SSE and maintains low interface resistance even after stripping a significant amount of Li without generating interface gaps. Thus, the dual-conductive framework enables solid Li anodes with improved capacity and lifespan, free from dendrite-induced short circuit or cell failure caused by interface detachment. The Li anode within the Li–Mg host melted on the garnet SSE exhibits excellent cycling stability for 500 h at 1 mA cm<sup>-2</sup> and an ensuing 500 h at 2 mA cm<sup>-2</sup>, totaling 750 mA h cm<sup>-2</sup> cumulative plating capacity, which is much higher than previous garnet-type all-solid-state Li batteries, without short circuiting or so-called soft short circuit. This strategy to dealloy Li from a Li–Mg alloy to form a dual-conductive framework opens a new way to construct safe, high-energy, and stable solid-state batteries.

## Experimental Section

**Synthesis of Garnet Electrolyte:** The Li<sub>6.75</sub>La<sub>3</sub>Zr<sub>1.75</sub>Ta<sub>0.25</sub>O<sub>12</sub> garnet-type SSE was synthesized via a conventional solid-state reaction method. Stoichiometric amounts of LiOH·H<sub>2</sub>O (99.9%, Sigma Aldrich), La<sub>2</sub>O<sub>3</sub> (≥99.9%, Sigma Aldrich), ZrO<sub>2</sub> (99.9%, Sigma Aldrich), and Ta<sub>2</sub>O<sub>5</sub> (99.9%, Sigma Aldrich) were adequately mixed in isopropyl alcohol (IPA) for 12 h. An additional 12 wt% excess LiOH·H<sub>2</sub>O was added to compensate for the loss of lithium volatilization during the subsequent high-temperature treatment, in which the mixed materials were dried and calcined at 920 °C for 12 h. The resulting powder was mixed with IPA and ball-milled for 9 h. After drying at room temperature, the powders were pressed into pellets with a diameter of 10 mm using a pressure of 300 MPa and then sintered at 1150 °C for 9 h. After the sintering process, the surfaces of the pellets were polished in a glove box in Ar atmosphere.

**Fabrication of Li–Mg Alloy Anode:** The Li–Mg alloy was made by melting Li-metal foil and Mg metal foil (mass ratio 4:1) at 350 °C for 30 min in an Argon-filled glove box (O<sub>2</sub> and H<sub>2</sub>O <0.1 ppm), followed by cooling to room temperature. Before melting the metals, the surface oxide layers were removed by scratching the surfaces of the Li and Mg metal foils. A piece of Li–Mg alloy (≈2 mg) was then placed on each side of the polished garnet pellet and heated at 350 °C for 30 min with a small amount of pressure. The garnet electrolyte was not treated by any surface coating, but was well wetted by the Li–Mg alloy. After cooling to room temperature, the Li–Mg alloy anode was solidified on the garnet pellet.

**Characterization and Electrochemical Tests:** Powder XRD was performed on a C2 Discover diffractometer (Bruker AXS) at 40 kV and 40 mA using a Cu Kα radiation source (λ = 1.54056 Å). SEM was conducted on a Hitachi SU-70 field emission SEM coupled with an EDX system for elemental analysis. The ToF-SIMS was collected using an attachment on the Tescan GAIA FIB/SEM with an ion beam at 30 kV and 1.8 nA.

Electrochemical analyses were performed with the solid-state batteries sealed in coin cells at room temperature. The Li–Mg | garnet SSE | Li–Mg symmetric cell was assembled with a conductive carbon sponge and sealed in a 2032-type coin cell by a crimping machine. Electrochemical stripping and plating tests of the solid-state cells were conducted on a LAND electrochemical testing system with galvanostatic conditions. The electrochemical impedance spectra were performed in a frequency range of 10 MHz–100 Hz with a voltage amplitude of 20 mV.



## Supporting Information

Supporting Information is available from the Wiley Online Library or from the author.

## Acknowledgements

C.Y. and H.X. contributed equally to this work. C.Y., K.F., and L.H. contributed to the idea. C.Y. conducted the electrochemical study and morphology observation. H.X. and W.P. synthesized the garnet electrolyte. B.L. conducted the XRD. J.R. and C.W. assisted in the ToF-SIMS characterization. J.D. contributed to the schematics. C.Y. and L.H. wrote the manuscript. All authors contributed to result analysis. This work was supported by the US Department of Energy Advanced Research Projects Agency–Energy (Contract DE-AR0000384) and Office of Energy Efficiency and Renewable Energy (Contract DE-EE0006860). The authors acknowledge the support of the Maryland Nanocenter, its Surface Analysis Center, and the AIMLab. W.P. acknowledges the financial support of China Scholarship Council (CSC No. 201706280132).

## Conflict of Interest

The authors declare no conflict of interest.

## Keywords

electron/ion dual-conductive frameworks, garnet-type electrolytes, lithium-metal anodes, lithium–magnesium alloys, solid-state batteries

Received: July 26, 2018  
Revised: October 14, 2018  
Published online:

- [1] a) D. Lin, Y. Liu, Y. Cui, *Nat. Nanotechnol.* **2017**, *12*, 194; b) J. W. Choi, D. Aurbach, *Nat. Rev. Mater.* **2016**, *1*, 16013.
- [2] W. Xu, J. Wang, F. Ding, X. Chen, E. Nasymbulin, Y. Zhang, J.-G. Zhang, *Energy Environ. Sci.* **2014**, *7*, 513.
- [3] a) X.-B. Cheng, R. Zhang, C.-Z. Zhao, Q. Zhang, *Chem. Rev.* **2017**, *117*, 10403; b) K. N. Wood, M. Noked, N. P. Dasgupta, *ACS Energy Lett.* **2017**, *2*, 664.
- [4] C. Yang, K. Fu, Y. Zhang, E. Hitz, L. Hu, *Adv. Mater.* **2017**, *29*, 1701169.
- [5] a) Q. Pan, D. M. Smith, H. Qi, S. Wang, C. Y. Li, *Adv. Mater.* **2015**, *27*, 5995; b) R. Khurana, J. L. Schaefer, L. A. Archer, G. W. Coates, *J. Am. Chem. Soc.* **2014**, *136*, 7395.
- [6] a) W. Liu, S. W. Lee, D. Lin, F. Shi, S. Wang, A. D. Sendek, Y. Cui, *Nat. Energy* **2017**, *2*, 17035; b) L. Chen, Y. Li, S.-P. Li, L.-Z. Fan, C.-W. Nan, J. B. Goodenough, *Nano Energy* **2018**, *46*, 176; c) Z. Tu, Y. Kambe, Y. Lu, L. A. Archer, *Adv. Energy Mater.* **2014**, *4*, 1300654; d) D. Zhou, R. Liu, Y.-B. He, F. Li, M. Liu, B. Li, Q.-H. Yang, Q. Cai, F. Kang, *Adv. Energy Mater.* **2016**, *6*, 1502214.
- [7] a) V. Thangadurai, H. Kaack, W. J. F. Weppner, *J. Am. Ceram. Soc.* **2003**, *86*, 437; b) R. Murugan, S. Ramakumar, N. Janani, *Electrochem. Commun.* **2011**, *13*, 1373; c) H. Kawai, J. Kuwano, *J. Electrochem. Soc.* **1994**, *141*, L78; d) Z. Liu, W. Fu, E. A. Payzant, X. Yu, Z. Wu, N. J. Dudney, J. Kiggans, K. Hong, A. J. Rondinone, C. Liang, *J. Am. Chem. Soc.* **2013**, *135*, 975; e) E. Rangasamy, Z. Liu, M. Gobet, K. Pilar, G. Sahu, W. Zhou, H. Wu, S. Greenbaum, C. Liang, *J. Am. Chem. Soc.* **2015**, *137*, 1384; f) F. Han, J. Yue, X. Zhu, C. Wang, *Adv. Energy Mater.* **2018**, *8*, 1703644; g) Y. Yan, R. S. Kühnel, A. Remhof, L. Duchêne, E. C. Reyes, D. Rentsch, Z. Łodziana, C. Battaglia, *Adv. Energy Mater.* **2017**, *7*, 1700294; h) M. Matsuo, A. Remhof, P. Martelli, R. Caputo, M. Ernst, Y. Miura, T. Sato, H. Oguchi, H. Maekawa, H. Takamura, *J. Am. Chem. Soc.* **2009**, *131*, 16389; i) J. Trevey, J. S. Jang, Y. S. Jung, C. R. Stoldt, S.-H. Lee, *Electrochem. Commun.* **2009**, *11*, 1830; j) Y. J. Nam, S.-J. Cho, D. Y. Oh, J.-M. Lim, S. Y. Kim, J. H. Song, Y.-G. Lee, S.-Y. Lee, Y. S. Jung, *Nano Lett.* **2015**, *15*, 3317; k) J. A. Dawson, P. Canepa, T. Famprikis, C. Masquelier, M. S. Islam, *J. Am. Chem. Soc.* **2018**, *140*, 362.
- [8] a) A. Manthiram, X. Yu, S. Wang, *Nat. Rev. Mater.* **2017**, *2*, 16103; b) J. Janek, W. G. Zeier, *Nat. Energy* **2016**, *1*, 16141.
- [9] a) V. Thangadurai, S. Narayanan, D. Pinzaru, *Chem. Soc. Rev.* **2014**, *43*, 4714; b) Y. Zhu, X. He, Y. Mo, *ACS Appl. Mater. Interfaces* **2015**, *7*, 23685.
- [10] a) C. Yu, S. Ganapathy, E. R. H. van Eck, H. Wang, S. Basak, Z. Li, M. Wagemaker, *Nat. Commun.* **2017**, *8*, 1086; b) W. D. Richards, L. J. Miara, Y. Wang, J. C. Kim, G. Ceder, *Chem. Mater.* **2016**, *28*, 266; c) R. Sudo, Y. Nakata, K. Ishiguro, M. Matsui, A. Hirano, Y. Takeda, O. Yamamoto, N. Imanishi, *Solid State Ionics* **2014**, *262*, 151; d) S. Xin, Y. You, S. Wang, H.-C. Gao, Y.-X. Yin, Y.-G. Guo, *ACS Energy Lett.* **2017**, *2*, 1385; e) P. Canepa, J. A. Dawson, G. Sai Gautam, J. M. Statham, S. C. Parker, M. S. Islam, *Chem. Mater.* **2018**, *30*, 3019.
- [11] a) X. Han, Y. Gong, K. Fu, X. He, G. T. Hitz, J. Dai, A. Pearse, B. Liu, H. Wang, G. Rubloff, Y. Mo, V. Thangadurai, E. D. Wachsman, L. Hu, *Nat. Mater.* **2017**, *16*, 572; b) W. Luo, Y. Gong, Y. Zhu, K. K. Fu, J. Dai, S. D. Lacey, C. Wang, B. Liu, X. Han, Y. Mo, E. D. Wachsman, L. Hu, *J. Am. Chem. Soc.* **2016**, *138*, 12258.
- [12] a) K. Fu, Y. Gong, Z. Fu, H. Xie, Y. Yao, B. Liu, M. Carter, E. Wachsman, L. Hu, *Angew. Chem., Int. Ed.* **2017**, *56*, 14942; b) C. L. Tsai, V. Roddatis, C. V. Chandran, Q. Ma, S. Uhlenbruck, M. Bram, P. Heitjans, O. Guillon, *ACS Appl. Mater. Interfaces* **2016**, *8*, 10617.
- [13] A. Sharafi, E. Kazyak, A. L. Davis, S. Yu, T. Thompson, D. J. Siegel, N. P. Dasgupta, J. Sakamoto, *Chem. Mater.* **2017**, *29*, 7961.
- [14] Y. Li, X. Chen, A. Dolocan, Z. Cui, S. Xin, L. Xue, H. Xu, K. Park, J. B. Goodenough, *J. Am. Chem. Soc.* **2018**, *140*, 6448.
- [15] S. Wang, H. Xu, W. Li, A. Dolocan, A. Manthiram, *J. Am. Chem. Soc.* **2017**, *140*, 250.
- [16] D. G. Kevorkov, J. Gröbner, R. Schmid-Fetzer, V. V. Pavlyuk, G. S. Dmytriv, O. I. Bodak, *J. Phase Equilib.* **2001**, *22*, 34.
- [17] C. Wang, H. Xie, L. Zhang, Y. Gong, G. Pastel, J. Dai, B. Liu, E. D. Wachsman, L. Hu, *Adv. Energy Mater.* **2018**, *8*, 1701963.
- [18] M. N. Obrovac, V. L. Chevrier, *Chem. Rev.* **2014**, *114*, 11444.
- [19] M. D. Tikekar, S. Choudhury, Z. Tu, L. A. Archer, *Nat. Energy* **2016**, *1*, 16114.
- [20] C. Wang, Y. Gong, B. Liu, K. Fu, Y. Yao, E. Hitz, Y. Li, J. Dai, S. Xu, W. Luo, E. D. Wachsman, L. Hu, *Nano Lett.* **2017**, *17*, 565.
- [21] Y. Gong, K. Fu, S. Xu, J. Dai, T. R. Hamann, L. Zhang, G. T. Hitz, Z. Fu, Z. Ma, D. W. McOwen, X. Han, L. Hu, E. D. Wachsman, *Mater. Today* **2018**, *21*, 594.
- [22] Y. Li, W. Zhou, X. Chen, X. Lü, Z. Cui, S. Xin, L. Xue, Q. Jia, J. B. Goodenough, *Proc. Natl. Acad. Sci. USA* **2016**, *113*, 13313.